DE GRUYTER Z. Phys. Chem. 2020; 234(4): 655–682

Martin Rohloff, Björn Anke, Dennis Wiedemann, Anna C. Ulpe, Olga Kasian, Siyuan Zhang, Christina Scheu, Thomas Bredow, Martin Lerch and Anna Fischer*

Synthesis and Doping Strategies to Improve the Photoelectrochemical Water Oxidation Activity of $BiVO_4$ Photoanodes

https://doi.org/10.1515/zpch-2019-1476
Received May 15, 2019; accepted October 1, 2019

Abstract: $BiVO_4$ is one of the most investigated and most promising metal oxide based photoanode materials for photoelectrochemical (PEC) water oxidation. Although it has several advantages (suitable band gap around 2.4 eV, suitable valence-band position for water oxidation, low toxicity, high abundance), it suffers from slow charge-carrier transport properties, high surface recombination, and limited water-oxidation activity. In the present work, we review the synthesis and doping strategies that we developed in the last years to improve the PEC performance of $BiVO_4$ photoanodes. Strategies ranging from single anion doping or cation doping to anion and cation co-doping will be presented for fluoride and molybdenum as anion and cation dopants, respectively. One major result is that co-doping allows combining the most important PEC specific benefits of each type of dopant, i.e. an increased charge-injection efficiency in case of fluoride as well as an increased charge-separation efficiency in case of molybdenum.

***Corresponding author: Anna Fischer,** University of Freiburg, Institute of Inorganic and Analytical Chemistry, Freiburg Institute for Interactive Materials and Bioinspired Technologies, Freiburg Materials Research Center, Freiburg 79104, Germany, e-mail: anna.fischer@ac.uni-freiburg.de. https://orcid.org/0000-0003-4567-3009
Martin Rohloff: University of Freiburg, Institute of Inorganic and Analytical Chemistry, Freiburg Institute for Interactive Materials and Bioinspired Technologies, Freiburg Materials Research Center, Freiburg 79104, Germany; and Technical University Berlin, Institute for Chemistry, 10623 Berlin, Germany
Björn Anke, Dennis Wiedemann and Martin Lerch: Technical University Berlin, Institute for Chemistry, 10623 Berlin, Germany. https://orcid.org/0000-0001-6294-3205 (D. Wiedemann); https://orcid.org/0000-0002-4065-4928 (M. Lerch)
Anna C. Ulpe and Thomas Bredow: University of Bonn, Mulliken Center for Theoretical Chemistry, Institute for Physical and Theoretical Chemistry, 53115 Bonn, Germany
Olga Kasian, Siyuan Zhang and Christina Scheu: Max-Planck-Institut für Eisenforschung GmbH, 40237 Düsseldorf, Germany. https://orcid.org/0000-0001-6315-0637 (O. Kasian), https://orcid.org/0000-0001-7916-1533 (C. Scheu)

Keywords: anion and cation co-doping; $BiVO_4$; Mo doping; O/F substitution; photoanodes.

1 Introduction

Photoelectrochemical (PEC) water splitting is considered one of the most elegant ways for sustainable hydrogen production. Sunlight, the most abundant renewable energy source, is converted by semiconductor electrodes into electric bias, which is used to split water directly into oxygen and hydrogen. Semiconductor materials that absorb a sufficient portion of solar light ($E_g \simeq 2.1$ eV), separate and transport the charge carriers efficiently, favor the water splitting half-reactions at the surface, and are stable in aqueous media under illumination are desired for the development of efficient PEC water-splitting devices [1].

In this context, $BiVO_4$ is one of the most promising electrode materials for the light-induced oxygen evolution reaction (OER). Due to its appropriate band gap ($E_g \simeq 2.4$ eV), its suitable valence-band edge position greater than the water oxidation potential (on the electrochemical scale), its non-toxicity, its low cost and abundance, $BiVO_4$ has become one of the most-investigated oxide-based photoanode materials for photoelectrochemical water oxidation [2–6].

From the theoretical point of view, monoclinic $BiVO_4$ (m-$BiVO_4$) has also gained a lot of attention in the last years. In particular, its outstanding electronic properties have been investigated. m-$BiVO_4$ was classified as a direct band-gap semiconductor with a valence band dominated by oxygen 2p states and a conduction band dominated by vanadium 3d states (Note: several energetically equivalent minima were found for the CB) [7]. The composition of valence and conduction bands was confirmed via density functional theory (DFT) computations carried out by Zhao et al. [8], who however classified the electronic band gap as indirect. This study also showed that the slightly distorted crystal structure of m-$BiVO_4$ determines not only its electronic structure but also its peculiar optical properties. Recently, a pronounced optical anisotropy was observed in the low-energy range between 2.0 and 2.7 eV [9].

Despite the numerous beneficial properties of $BiVO_4$ for application as anode material in photoelectrochemical water splitting, there are some performance-limiting properties, which have to be optimized in that context. As shown by Abdi et al. [10], sluggish bulk electronic conductivity is one of the main performance bottlenecks of $BiVO_4$-based photoelectrodes – a problem, which can be overcome, e.g. *via* doping strategies. A wide variety of dopants has been suggested based on computation. For example, a DFT study of doping effects in $BiVO_4$ indicates that transition metal doping could reduce the effective hole mass on the valence-band top [11]. A more recent DFT study shows that excellent n-type conductivity can be realized *via* Mo or W doping at O-poor growth conditions [12]. A DFT + U study carried out in 2016 showed that W-doped $BiVO_4$ has a smaller band gap than Mo-doped $BiVO_4$ [13]. The enhanced photocatalytic activity of Mo-doped $BiVO_4$ is attributed to the facilitated charge-carrier separation as well as an introduction of surface oxygen quasi-vacancies [14]. Improved PEC water oxidation performance of doped $BiVO_4$ photoanodes has also been demonstrated in practice [15–19]. In addition, several post-synthetic treatments have been developed in recent years to further improve the performance of $BiVO_4$ photoanodes [20, 21].

Since monoclinic $BiVO_4$ is discussed as photoanode material for photoelectrochemical water oxidation, the surface and water adsorption properties are of particular interest. Comprehensive DFT calculations for several low-index surfaces of monoclinic $BiVO_4$ reveal that, in the most stable surface terminations, the V atoms are fully coordinated, while dangling bonds are derived from broken Bi–O connections [22]. Therefore, the thermodynamically most stable surfaces are the (010), (110), and $(11\bar{1})$ planes. The water adsorption properties of m-$BiVO_4$ were investigated by Oshikiri and Boero in 2006 [23]. According to their first-principles molecular dynamics simulations, water is molecularly adsorbed at the five-fold-coordinated Bi surface sites with an adsorption energy of *ca.* 0.58 eV per molecule, inducing a band-gap narrowing of *ca.* 0.2 eV.

In the present work, we review and discuss the different doping strategies – anion doping, cation doping as well as anion and cation co-doping – we applied for the stepwise improvement of the PEC performance of $BiVO_4$-based photoanodes.

First we performed anion doping, i.e. partial O/F substitution *via* a solid–gas reaction with HF formed *in situ*, and showed that it was effected in highly crystalline m-$BiVO_4$ powder samples [24]. Fluorine-containing $BiVO_4$ (F:$BiVO_4$) was characterized chemically, structurally, optically, and by means of quantum-chemical modeling, revealing that partial O/F substitution is concomitant with cation vacancy formation and optical bad-gap narrowing. Electrophoretic deposition further enabled the assembly of F:$BiVO_4$ particulate photoanodes on fluorine-doped tin-oxide (FTO) substrates and we could reveal a positive impact of partial O/F substitution on the PEC water-oxidation performance of F:$BiVO_4$.

Aiming at an improvement of the photoelectrode design, from a particulate to a continuous thin film structure, a new solution-based bottom-up approach was developed by us for the direct deposition via dip coating of $BiVO_4$ thin films [18]. The new protocol allows adjustment of the photoanode design to the material's properties to reach high PEC performance already for undoped $BiVO_4$ thin films. Fluorination (with slightly adjusted conditions to thin films) was also applied to the $BiVO_4$ thin-film photoanodes resulting – in line with our previous results – in an improved PEC water oxidation performance, which could be related to an enhanced hole transfer efficiency, i.e. improved water oxidation catalysis [25].

Further improvement of the PEC performance for water oxidation of these $BiVO_4$ thin-film photoanodes could be achieved by cation doping (i.e. molybdenum, Mo:$BiVO_4$) along with morphology and other PEC-relevant property optimization [18].

Finally, the concepts of anion and cation substitution were combined by us to form fluorine and molybdenum co-doped $BiVO_4$ thin-film photoanodes (F/Mo:$BiVO_4$) [25]. Systematic analysis of the charge separation and charge injection efficiencies revealed that the concomitant combination of anion and cation doping allows combining the enhanced charge separation efficiency of the molybdenum doping with the improved charge injection efficiency of the fluorine doping in one material system, thereby reaching the highest PEC water oxidation performance amongst all investigated systems.

2 O/F substitution in $BiVO_4$ powder

2.1 Synthesis

F:$BiVO_4$ highly crystalline powders were prepared as phase-pure material via a solid–vapor reaction using an indirect gas-flow apparatus (see Figure 1). Highly crystalline $BiVO_4$ powder, with particle sizes between several hundreds of nanometers to several micrometers, was loaded into a small corundum boat placed inside a larger one containing varying amounts of polyvinylidene fluoride (PVDF). As described in one of our earlier contributions [24], this arrangement advantageously prevents contact between the reagents in either solid or liquid form. The whole apparatus was placed inside a small corundum tube with one closed end and then put in a horizontal tube furnace. After treatment at 380 °C

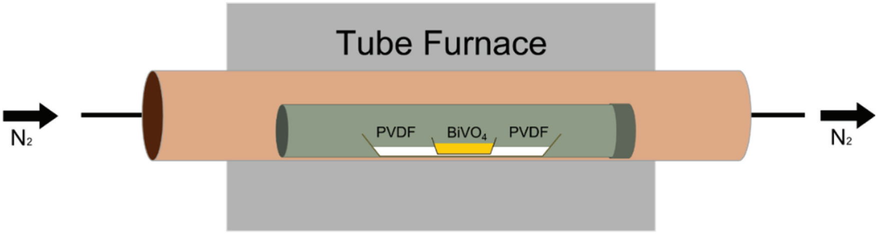

Fig. 1: Schematic of the fluorination apparatus. The inner corundum boat contains pristine $BiVO_4$ powder and the outer one is filled with varying amounts of PVDF [22].

for 24 h, a final heating step was performed in air at 450 °C for 30 min, leading to a highly crystalline orange powder, with particle sizes in the same size range as the starting $BiVO_4$ particles (SEM results in SI [24]). The ratio of bismuth to vanadium was confirmed via optical emission spectroscopy with inductively coupled plasma (ICP-OES; $r(\mathrm{Bi/V}) = 0.999{:}1$). The oxygen contents of pristine $BiVO_4$ and $F{:}BiVO_4$ were determined via hot-gas extraction ($BiVO_4$: 19.7 wt%; $F{:}BiVO_4$: 18.2 wt%).

2.2 Crystal-structural and optical characterization

Rietveld refinements of $BiVO_4$ and $F{:}BiVO_4$ model powders were started from the parameters reported for the clinobisvanite-type structure of $BiVO_4$ (space-group type: $I2/b$, JCPDS 14-0688) [26]. The results clearly demonstrate that fluorine incorporation does not change the structure type as seen in Figure 2. Figure 3 depicts the X-ray powder diffraction pattern of $F{:}BiVO_4$ along with the results of Rietveld refinement.

Density measurements as well as the results of the Rietveld refinement point to the formation of cation vacancies due to fluorination. This type of defect (cation vacancies/fluorine on oxygen positions) can be described using the following equation in the notation of Kröger and Vink [27]:

$$\mathrm{Bi}_{\mathrm{Bi}}^{\times} + \mathrm{V}_{\mathrm{V}}^{\times} + 8\ \mathrm{O}_{\mathrm{O}}^{\times} + 8\ \mathrm{HF} = V_{\mathrm{Bi}}^{'''} + V_{\mathrm{V}}^{'''''} + 8\ \mathrm{F}_{\mathrm{O}}^{\bullet} + \mathrm{BiVO_4(sf)} + 4\ \mathrm{H_2O}$$

A chemical composition of $Bi_{0.94}V_{0.94}O_{3.54}F_{0.46}$ was calculated with the experimentally determined oxygen content of 18.2 wt%, respecting the results of the Rietveld refinement, the measured density, and the proposed defect model.

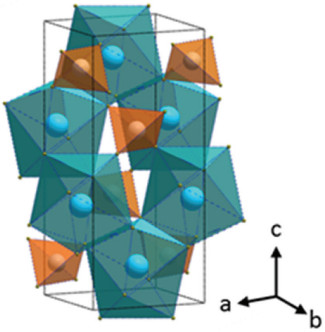

Fig. 2: Crystal structure of $F{:}BiVO_4$ in polyhedral representation ($Bi[O,F]_8$ polyhedra in blue, $V[O,F]_4$ tetrahedra in orange, unit cell in black).

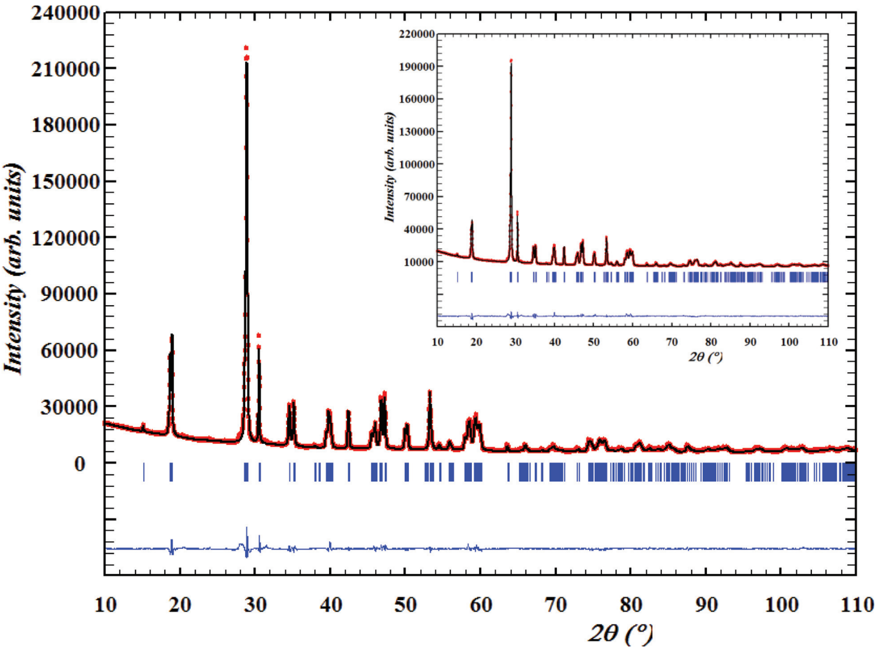

Fig. 3: X-ray powder diffraction patterns of F:BiVO$_4$ (inset: BiVO$_4$) with the result of the Rietveld refinement (observed pattern in red, calculated pattern in black, difference in blue).

The reaction energies of different defect models were calculated at the DFT level [4] using the projector-augmented wave method GPAW [28–30] and the PBE + U approach [31]. The most stable defect configurations (denoted as models A1 and A2, see Figure 4) closely correspond to the defect model that has been proposed above. However, instead of all fluorine atoms occupying the former oxygen sites as suggested by the Kröger–Vink notation, four F atoms are located on an interstitial position very close to a former oxygen position. This defect structure can be described as:

$$\mathrm{Bi}_{\mathrm{Bi}}^{\times} + \mathrm{V}_{\mathrm{V}}^{\times} + 8\ \mathrm{O}_{\mathrm{O}}^{\times} + 8\ \mathrm{HF} = V_{\mathrm{Bi}}^{'''} + V_{\mathrm{V}}^{'''''} + 4\ V_{\mathrm{O}}^{\bullet\bullet} + 4\ \mathrm{F}_{\mathrm{i}}^{'} + 4\ \mathrm{F}_{\mathrm{O}}^{\bullet} + \mathrm{BiVO_4(sf)} + 4\ \mathrm{H_2O}$$

In addition to the aforementioned defects, additional defects associated with free electrons explaining the n-type behavior of BiVO$_4$ and F:BiVO$_4$ (Mott-Schottky analysis vide infra) must be present in the system. The most likely explanation would be oxygen loss leading to the release of free electrons as detailed below for:

$$\mathrm{BiVO_4}:\quad \mathrm{O}_{\mathrm{O}}^{\times} = V_{\mathrm{O}}^{\bullet\bullet} + 0.5\ \mathrm{O_2} + 2\ \mathrm{e}'$$

$$\mathrm{F{:}BiVO_4}:\quad 2\ \mathrm{O}_{\mathrm{O}}^{\times} + 2\ \mathrm{HF} = 2\ \mathrm{F}_{\mathrm{O}}^{\bullet} + \mathrm{H_2O} + 0.5\ \mathrm{O_2} + 2\ \mathrm{e}'$$

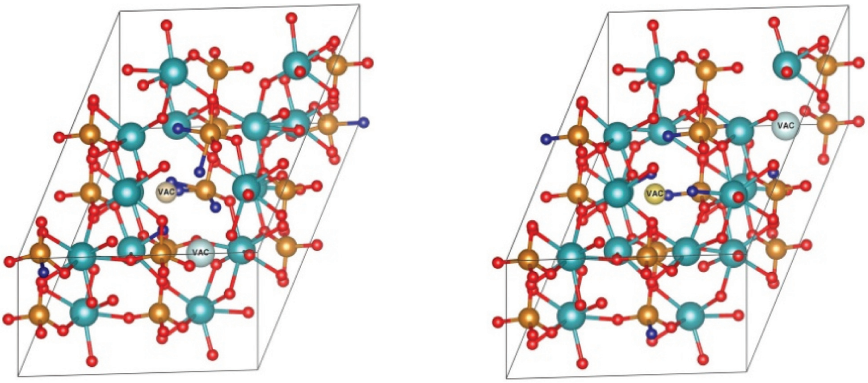

Fig. 4: F:$BiVO_4$ models A1 (left) and A2 (right) after structure relaxation. Bi: blue, V: orange, O: red, F: dark blue. Vanadium and bismuth vacancies are labeled with “VAC”, oxygen vacancies are not shown for clarity.

The optical absorbance of a semiconductor plays an important role in its photoelectrochemical behavior [32]. The optical spectra of orange-colored F:$BiVO_4$ and yellow $BiVO_4$ were measured in diffuse reflectance geometry. The results are plotted using the derivation of absorption spectrum fitting (DASF) method [33] in order to estimate the optical band gap (see Figure 5). For comparison a Tauc plot was also constructed (see data in [24]), yielding to similar results. The optical band gap for pristine $BiVO_4$ was determined as 2.42 eV, which is in good agreement with literature values [34]. The value for the partially O/F substituted material is slightly reduced to 2.39 eV. This small band-gap narrowing, also found in the contributions of Li et al. [35] and Jiang et al. [36], is beneficial in terms of

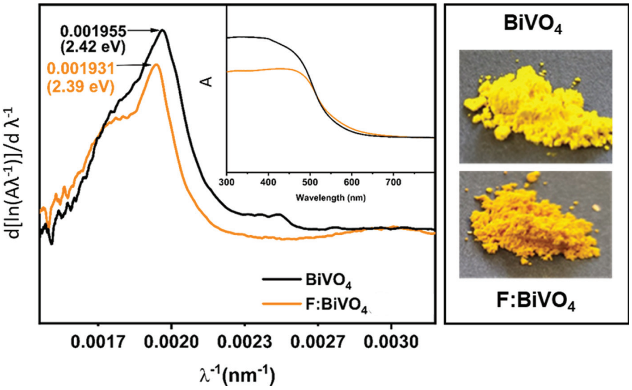

Fig. 5: Plot of d[ln(A/λ)]/d(1/λ) vs. (1/λ) for F:$BiVO_4$ (orange curve) and $BiVO_4$ (black curve); inset: diffuse reflectance spectra of both samples [35].

light absorption (shift of the absorption edge from 512 to 519 nm upon fluorine incorporation).

To investigate the optical properties of fluorine substituted $BiVO_4$, optical spectra of the two most stable defect models (denoted as A1 and A2, see [37]) were calculated using the GLLB-sc functional [38] and subsequently solving the Bethe–Salpeter equations [39]. The calculated imaginary part of the dielectric function in dependency on the photonic energy is shown in Figure 6.

While the first maximum for $BiVO_4$ is located at 2.41 eV, the first maximum for F:$BiVO_4$ is located at 2.07 eV and 1.98 eV for model A1 and A2, respectively. The difference between the maxima found for $BiVO_4$ and F:$BiVO_4$ is 0.34 eV and 0.43 eV for model A1 and A2, respectively. This difference is larger than the one determined from the experimental spectra (Figure 5). Nevertheless, the experimentally observed trend – a band gap reduction due to O/F substitution – is correctly reproduced by the theoretical models.

Additionally, we have calculated the electronic band structure and the projected density of states for $BiVO_4$ and F:$BiVO_4$ (model A1) with the crystalline orbital program CRYSTAL17 [40]. We have applied a self-consistent dielectric-dependent hybrid approach [41] based on the PW1PW hybrid functional [42]. In previous studies, it was shown that these methods provide electronic properties with accuracies comparable to more demanding Greens function techniques [43]. The atomic basis sets were of triple-zeta plus polarization quality [44, 45].

In agreement with previous theoretical investigations [7, 14, 46], stoichiometric $BiVO_4$ is an indirect semiconductor. According to our assignment of the special *k* points, the valence band maximum (VBM) is located between Γ and B and the conduction band minimum (CBM) is between B and A. The calculated indirect

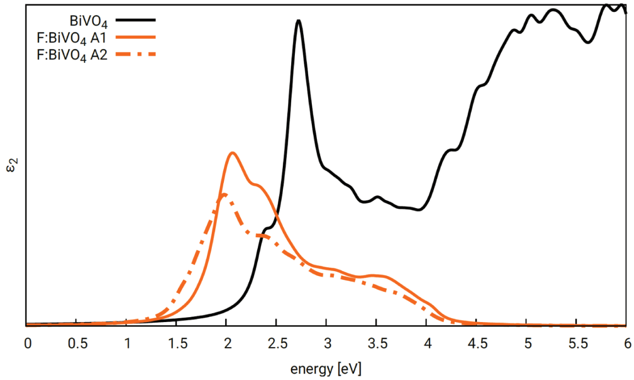

Fig. 6: Imaginary part of dielectric constant in dependency on the photonic energy (in eV) for F:$BiVO_4$ (orange) and $BiVO_4$ (black) [35].

band gap is 2.60 eV, slightly larger than the calculated optical gap (2.41 eV). Here, it should be noted that the electronic gap does not consider excitonic effects. The upper part of the VB is dominated by O 2p orbitals, while the lower part of the CB mainly consists of V 3d orbitals.

The calculated electronic structure for F:$BiVO_4$ defect model A1 is shown in the right-hand side of Figure 7. F:$BiVO_4$ is still an indirect semiconductor, but the highest occupied and lowest unoccupied bands are very flat, indicating an

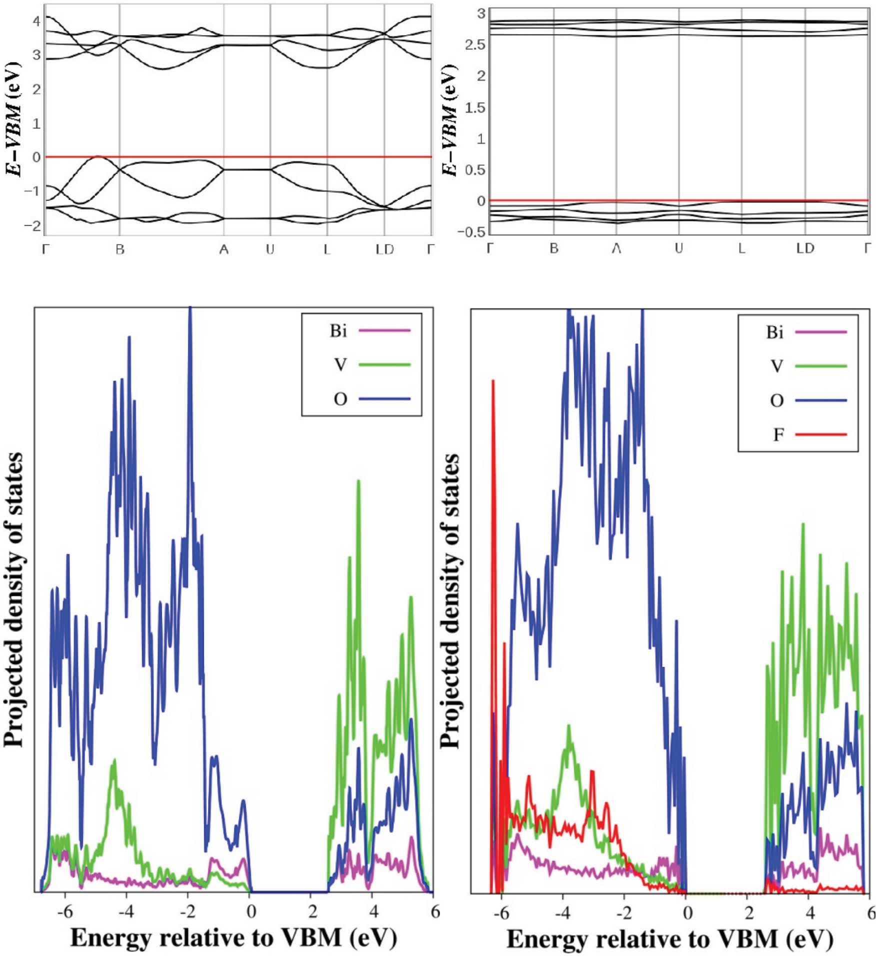

Fig. 7: Band structure and PDOS for $BiVO_4$ (left); and F:$BiVO_4$ model A1 (right); both calculated with a self-consistent variant of the PW1PW hybrid method. The special *k* points were assigned for the conventional Brillouin zone by means of the Bilbao crystallographic server [47–49]. In the band structures, the maximum of the valence band is set to zero.

increase of both the electron and hole effective masses. The fluorine 2p orbitals dominate the lower part of the VB and have only small contributions to the VB top. In addition, the composition of the CB bottom is only slightly modified. Accordingly, the calculated electronic band gap of F:$BiVO_4$ is similar to $BiVO_4$, 2.62 eV. However, there are significant contributions from O 2p and F 2p orbitals in the lowest CB levels in F:$BiVO_4$, which could explain why the calculated optical excitation energy is smaller in case of F:$BiVO_4$ than for the undoped system. It has to be noted that an earlier DFT study [46] came to different conclusions for the electronic structure. However, in that study a different defect model was assumed.

2.3 Investigation of PEC water oxidation properties of $BiVO_4$ and F:$BiVO_4$ powder electrodes

To investigate the photoelectrochemical properties of $BiVO_4$ and fluorinated $BiVO_4$ (F:$BiVO_4$) samples, photoanodes were fabricated from the pristine and fluorinated $BiVO_4$ powders via electrophoretic deposition (EPD) on FTO-coated glass slides as reported in one of our recent publications [24]. In both cases, percholated particulate films of similar thickness (in the µm range) were obtained on the FTO substrates. A thermal annealing between 450 °C and 550 °C after the EPD procedure strongly improved the PEC performance of the films, due to improved inter-particulate contact.

The PEC investigation shown in this work (powder electrodes [24] and thin film electrodes (vide infra) [18, 25]), were all done in the same set-up, consisting of a home-made PEC cell, with the $BiVO_4$ photoanode as working electrode, a Pt mesh as counter electrode and a RHE electrode as reference electrode. As electrolyte 0.1 M KPi buffer pH 7.3 was used. The photoanodes were illuminated by a 150 W Xe-lamp at a spectral range of 400–700 nm in all cases. The light intensity at the electrode surface was adjusted to 100 mW/cm^2 using a Si-diode light meter. If not stated otherwise, backside illumination (i.e. illumination via the FTO-coated glass side of the $BiVO_4$ photoanode) was used.

Current density-Voltage j-V curves of $BiVO_4$ and F:$BiVO_4$ electrodes prior and after deposition of a water-oxidation catalyst comprised of an amorphous cobalt phosphate species (CoPi) reported by Kanan and Nocera [50] along with photocurrent-transient measurements and Mott–Schottky analyses are shown in Figure 8. As can be seen in Figure 8a, higher photocurrents and improved photoelectrochemical water oxidation performance were observed for F:$BiVO_4$ in comparison to pristine $BiVO_4$, be it without or with CoPi surface modification. Note: For both types of electrodes ($BiVO_4$ and F:$BiVO_4$) the particle size distribution was broad and comparable, ranging from particles of several hundred of nanometers

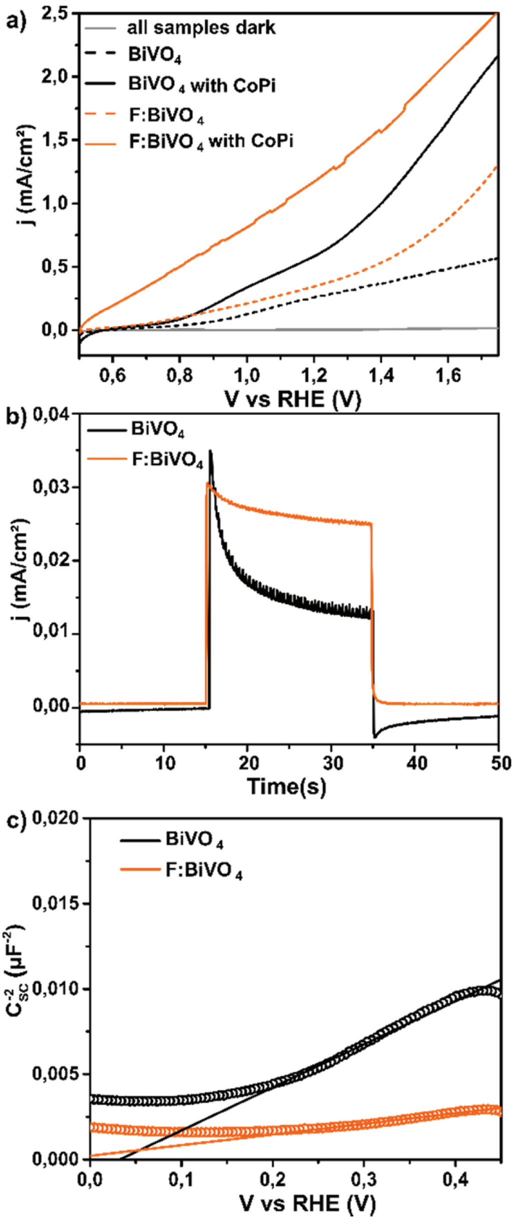

Fig. 8: (Photo-)Electrochemical investigations of pristine and fluorine-containing $BiVO_4$ and $F:BiVO_4$ electrodes: (a) *j*-*V* curves (0.1 m potassium phosphate buffer, pH 7.3, 400–700 nm, 100 mW/cm^2), (b) phototransient measurements, light on/off (0.1 m potassium phosphate buffer, pH 7.3, 440 nm, 2 mW/cm^2) at an applied Potential of 1.23 V vs. RHE, and c) Mott–Schottky plots of $BiVO_4$ and $F:BiVO_4$ at 1 kHz (0.5 m potassium phosphate buffer, pH 7.3).

to particles of several micrometers in size, so that simple particle size effects on the PEC performance could be discarded.

As can be seen in Figure 8b, the photocurrent transients of $BiVO_4$ exhibit pronounced photocurrent spikes when the light is switched on followed by a decrease/decay of initial photocurrent. When switching off the light, a less pronounced cathodic photocurrent overshoot is observed. This behavior generally points towards surface recombination [51–53]. In case of $F{:}BiVO_4$ photoanodes, the current spikes are far less pronounced – an indication for decreased surface recombination rates and likely enhanced hole transfer rates. These findings are in good agreement with literature reports assigning the improved PEC performance of $F{:}BiVO_4$ to the high electronegativity of fluorine. According to DFT calculations by Wen et al., adsorption of water molecules is facilitated at the fluorinated $BiVO_4$ surface due to the formation of strong $F \cdots H$ bonds [46]. In addition, according to Li et al., fluorination of $BiVO_4$ could result in F-related electron trap states leading to restrained recombination of photo-generated electron–hole pairs at the surface [35].

To further clarify the origin of the improved photoelectrochemical performance of $F{:}BiVO_4$, Mott–Schottky-type potentio-electrochemical impedance spectroscopy measurements for both materials were performed (see Figure 8c). For the pristine $BiVO_4$, a flat-band potential of $E_{FB} = 0.03$ V vs. the reversible hydrogen electrode (RHE) was obtained. The E_{FB} of $F{:}BiVO_4$ was determined to be slightly lower at $E_{FB} = -0.06$ V. Our results show a negative shift of the flat-band potential of about 0.1 V upon fluorine incorporation. The positive slope of the linear range in the Mott–Schottky plot indicates that both $BiVO_4$ and $F{:}BiVO_4$ are n-type semiconductors. A much smaller slope is observed for $F{:}BiVO_4$ than for pristine $BiVO_4$, indicating a higher carrier concentration – assuming a comparable surface area of the electrodes, identical amounts of deposited powder, and similar electrolyte exposed electrode areas of 0.5 cm^2.

To summarize, fluorine incorporation in $BiVO_4$ leads to an improvement of the PEC water oxidation performance due to a slightly decreased optical bandgap, a cathodically shifted flat-band potential, a higher number of free charge carriers, and favorable surface kinetics. However, observed water oxidation photocurrents for the EPD-processed powder electrodes are low compared to the highest reported photocurrent values for $BiVO_4$ photoanodes [16, 54, 55] but are fully in line with photocurrents achieved for comparable EPD-processed $BiVO_4$ electrodes (about 0.6 mA/cm^2) [56, 57]. Low photocurrents of the EPD-based electrodes are probably caused by unfavorable electrode design in terms of particle size (micrometer sized particles, percolated morphology, film thickness, etc.).

To exercise maximum control over electrode design/morphology, a new wet chemical synthesis method was developed for the synthesis of $BiVO_4$ based thin films.

3 Optimization of $BiVO_4$ thin film photoanodes

3.1 $BiVO_4$ thin film electrodes

Our novel, non-aqueous, wet chemical synthesis method is based on metalorganic precursors of bismuth and vanadium using chloroform as a solvent [18]. The synthesis steps are depicted schematically in Figure 9.

As emphasized by the group of Vest, metal hexanoates are suitable compounds for the solution-based synthesis of metal oxide thin films, because they are quantitatively transformed into metal oxides when pyrolized [58]. However, for a bimetallic compound like $BiVO_4$, the exclusive use of metal hexanoates is not appropriate, because metal hexanoates usually do not bind to each other when mixed together. Hence, they need to be mixed with other metal precursors. According to Lange, usage of metal alkoxides and hexanoates results in the formation of "hybrid-alkoxide" precursors with defined cation ratios [59]. This synthesis concept was adapted for the synthesis of $BiVO_4$, i.e. bismuth 2-ethylhexanoate and vanadium oxytriethoxide were mixed to form a bismuth vanadium hybrid-alkoxide precursor. The precursor solution was used for dip-coating FTO substrates resulting in an amorphous Bi- and V-containing thin film. The as-prepared thin film was calcined in air at 450 °C leading to crystalline $BiVO_4$ thin films.

Structural characterization by means of gracing-incidence X-ray diffraction (GI-XRD) revealed the thin films to crystallize in the clinobisvanite structure. Furthermore, via UV/Vis spectroscopy, an optical bandgap of ca. 2.4 eV was estimated [18]. To investigate the morphology of the $BiVO_4$ thin films, several electron microscopy methods were applied. By means of scanning electron microscopy (SEM), morphological features, which are summarized in Figure 10, could be

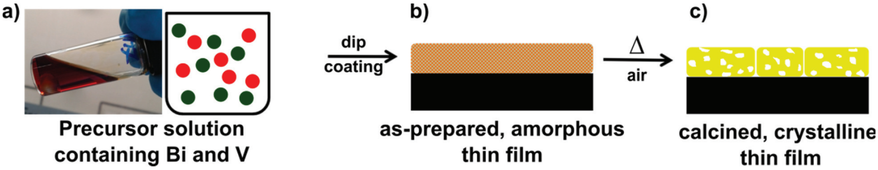

Fig. 9: Synthesis scheme: (a) precursor solution, (b) as-deposited amorphous thin film, and (c) calcined, crystalline $BiVO_4$ thin film. Adapted from ref. [18] with permission from The Royal Society of Chemistry.

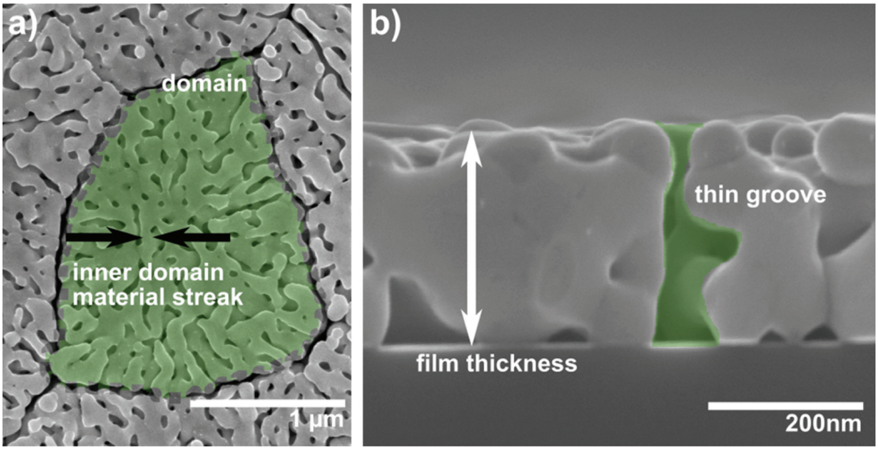

Fig. 10: Illustration of discussed thin film features, highlighted in (a) an SEM top view image and (b) a cross section image of a 5% Mo:$BiVO_4$ thin film on a Si substrate. Adapted from ref. [18] with permission from The Royal Society of Chemistry.

identified. $BiVO_4$ thin films (and those of its doped analogues, vide infra) consist of differently sized porous areas (green areas in Figure 10a, referred to as domains) separated from each other by thin grooves (green areas in Figure 10b). As revealed by SEM cross-section images, the thin grooves separating the porous domains run throughout the entire film down to the substrate. It was demonstrated via transmission electron microscopy (TEM), selected-area electron diffraction (SAED), and electron backscatter diffraction (EBSD) investigations (data shown in ref. [18]) that every domain exhibits a preferred orientation and that the orientations of each domain are different. Within a domain, worm-like pores of several tens of nanometers are enclosed by thin-film material referred to as "inner-domain material streak" (areas delimited by arrows in Figure 10a). In case of the undoped $BiVO_4$ thin films, the inner-domain material-streak size is lower than the minority-carrier diffusion length of $BiVO_4$ (approximately 70 nm), which is favorable for applications in PEC water oxidation.

$BiVO_4$ thin films synthesized according to the described method were applied for PEC water oxidation. *j-V* curves are shown in Figure 11a. Observed photocurrents of the pristine $BiVO_4$ thin films are low in front-side illumination (illumination via the $BiVO_4$ layer) and slightly higher in backside illumination (illumination via the FTO layer), respectively. This result is believed to indicate a strong limitation of the PEC performance due to limited electron-hole separation and slow electron migration to the conductive FTO back contact [60]. More precisely, this difference is believed, according to Xiao et al., to result from a fast

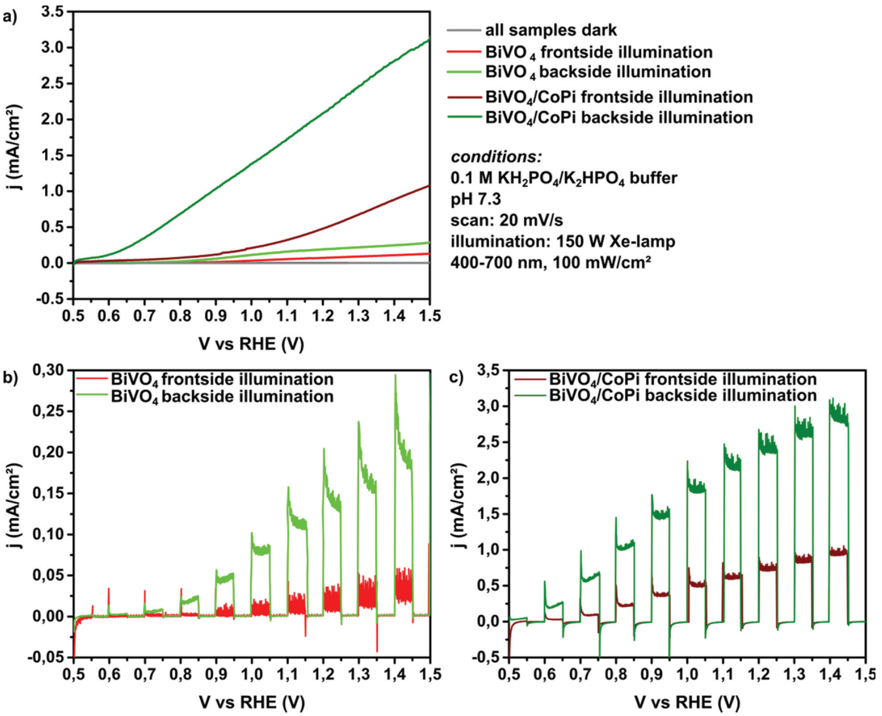

Fig. 11: (a) *j*-*V* curves of $BiVO_4$ thin films with and without a layer of CoPi water oxidation catalyst under continuous illumination, *j*-*V* curves of $BiVO_4$ thin films (b) without and (c) with a layer of CoPi water oxidation catalyst under chopped illumination.

trap-free electron diffusion mode occurring under back-side illumination (due to filled trapped states in the region proximal to the FTO substrate) and a trap-limited transport occurring under front-side illumination leading to higher recombination probability and decreased charge separation [60]. Depositing a thin layer of CoPi water oxidation catalyst enhances the photoelectrochemical performance and observed photocurrents. With CoPi deposited, photocurrents of 0.5 mA/cm^2 at 1.23 V vs. RHE were observed in front-side illumination, while backside illumination yielded photocurrents of 2.1 mA/cm^2 at 1.23 V vs. RHE. We could show, in line with literature, that deposition of CoPi water oxidation catalyst reduces surface recombination, slightly improves water oxidation kinetics, and therefore enhances the overall photoelectrochemical performance of the $BiVO_4$ thin films (vide infra).

The *j*-*V* curves under chopped illumination presented in Figure 11b and c additionally reveal a “spike-and-overshoot” behavior, which qualitatively indicates surface recombination of photo-generated charge carriers to be a PEC performance-limiting factor even after surface modification with CoPi.

The results indicate charge separation and charge transport through the electrode to be limiting the overall PEC water oxidation performance. For this reason, efficient doping strategies to improve charge carrier transport were combined with the $BiVO_4$ thin-film synthesis approach described here allowing morphology fine-tuning of doped $BiVO_4$ thin films.

3.2 Fluorinated $BiVO_4$ thin film electrodes

The soft fluorination method developed for $BiVO_4$ powders was slightly adjusted to realize fluorine incorporation in $BiVO_4$ thin films, further referred to as F:$BiVO_4$ thin films. Briefly explained, in a first step, the $BiVO_4$ thin films were synthesized via the above-explained thin film deposition approach and were subsequently fluorinated according to the soft fluorination method (vide supra). The detailed synthesis procedure has been published recently [25].

Structural analysis in terms of GI-XRD did not reveal any significant influence of the fluorine incorporation on the structure type of the $BiVO_4$ thin films within the resolution limits of this method and the equipment. Furthermore, investigation of the optical absorption properties revealed a slight decrease of the optical bandgap by fluorine incorporation – a result, which matches the trend observed for the $BiVO_4$ and fluorine-containing $BiVO_4$ powder samples.

In order to gain information about the F content within the film samples, lamellae were cut out of the thin films by means of a focused ion beam (FIB) procedure and investigated by scanning transmission electron microscopy (STEM) and energy-dispersive X-ray spectroscopy (EDX). Integration over the F–K spectral window shows counts in the F:$BiVO_4$ and F/Mo:$BiVO_4$ thin films as well as their non-fluorinated counterparts, due to the presence of an escape peak artefact. Once the Bi-L_α X-rays with an energy of 2.42 keV hit the silicon drift detector in the EDX spectrometer, a tiny fraction excites a Si 1s electron and loses 1.74 keV energy. The remaining energy of 0.68 keV was recorded as an escape peak, which overlaps with the F-K_α line at 0.69 keV. In view of these results, EDX is not a suitable technique to identify fluorine in a Bi-rich matrix.

For this reason, X-ray photoelectron spectroscopy (XPS) was carried out to identify fluorine within the fluorinated $BiVO_4$ thin films. As can be seen in Figure 12, fluorine could be traced in the F:$BiVO_4$ thin film sample while bismuth, vanadium, and oxygen peaks remain unchanged.

Via SEM analysis (see Figure 13) of the F:$BiVO_4$ thin films, it was demonstrated that the fluorination procedure only slightly effects the thin film morphology.

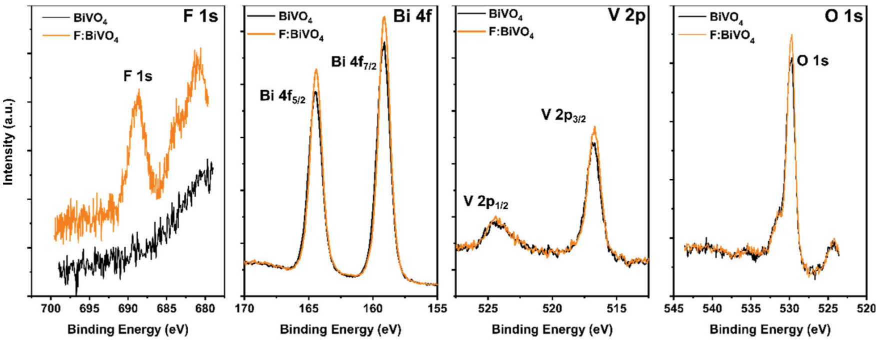

Fig. 12: XPS spectra of $BiVO_4$ and F:$BiVO_4$ thin film samples. Adapted with permission from ref. [23]. Copyright 2019 American Chemical Society.

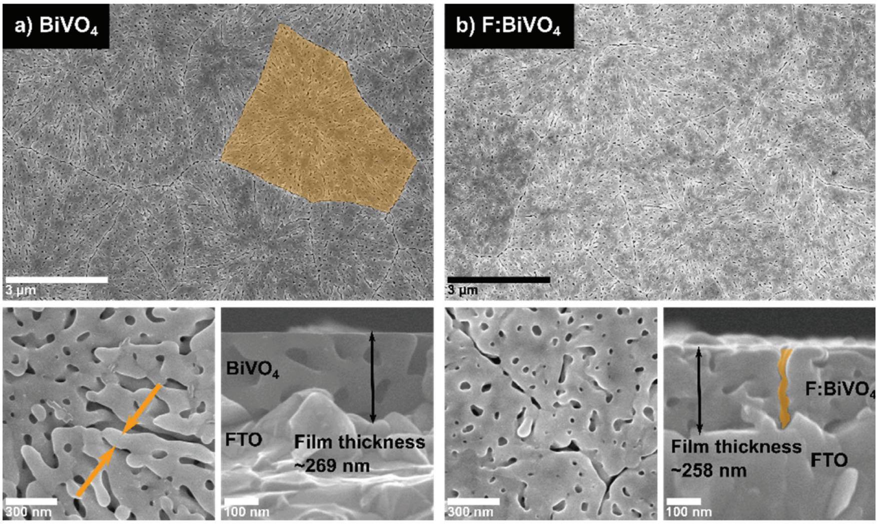

Fig. 13: SEM top view and cross sectional images of (a) $BiVO_4$ and (b) fluorinated $BiVO_4$ thin films on FTO substrate. Adapted with permission from ref. [25]. Copyright 2019 American Chemical Society.

Material densification/sintering was observed accompanying the additional heat treatments of the fluorination.

Investigations of the pristine $BiVO_4$ thin film photoanodes and their fluorinated counterpart with and without CoPi under illumination in front-side and backside mode are shown in Figure 14. As can be seen for $BiVO_4$ and F:$BiVO_4$ samples without surface modification (see Figure 14a), obtained photocurrents are slightly higher for the fluorinated samples. Photocurrents obtained in front-side

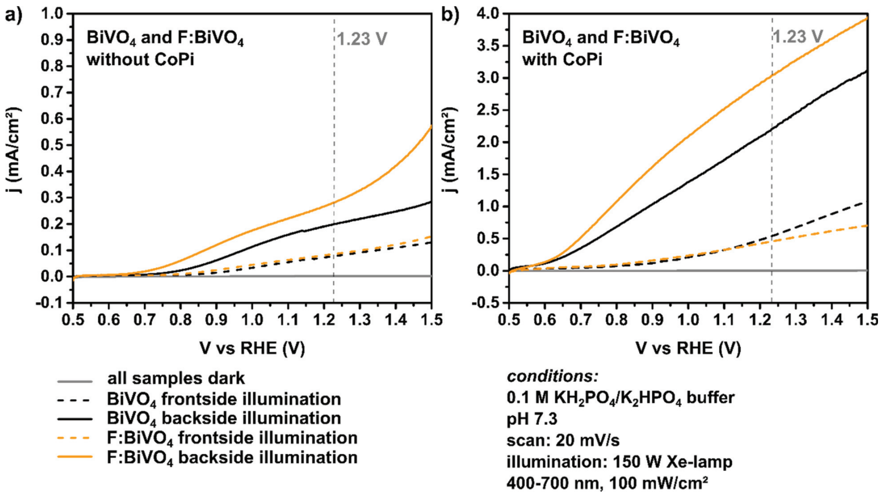

Fig. 14: *j*-*V* curves of $BiVO_4$ and fluorinated $BiVO_4$ thin film photoanodes (a) without CoPi deposited and (b) with CoPi. Adapted with permission from ref. [25]. Copyright 2019 American Chemical Society.

illumination vary only little for the pristine and the fluorinated $BiVO_4$ thin films. Using backside illumination results in higher photocurrents and a bigger difference between the pristine $BiVO_4$ and its fluorinated counterpart. Photocurrents after deposition of a thin layer of CoPi on the electrodes' surfaces are shown in Figure 14b. Very similar photocurrents are observed when front-side illumination is used. Application of backside illumination results in significantly higher photocurrents. The fluorinated sample yields a maximum photocurrent of 3.03 mA/cm^2 at 1.23 V vs. RHE, which is by 0.8 mA/cm^2 higher than for its pristine counterpart yielding only 2.20 mA/cm^2 at 1.23 V vs. RHE. The difference in photocurrents depending on the illumination mode remains upon CoPi deposition.

Photocurrent transients' measurements of the $BiVO_4$ and $F:BiVO_4$ thin film electrodes are shown in Figure 15. The photocurrent transients of both samples exhibit significant spikes (light on). While a pronounced overshoot is observed for the pristine $BiVO_4$ sample, a reduced overshoot is observed for the fluorinated sample when switching off the light, indicating less hole accumulation at the surface. As already elucidated, the pristine $BiVO_4$ thin film photoanode suffers from surface recombination (vide supra) and insufficient hole transfer. In comparison with the pristine $BiVO_4$ sample, transient analysis for the fluorinated $BiVO_4$ reveals a reduced surface recombination and an improved hole transfer [25]. As suggested by Li et al. [35] surface-bound fluorine induces electron traps, which

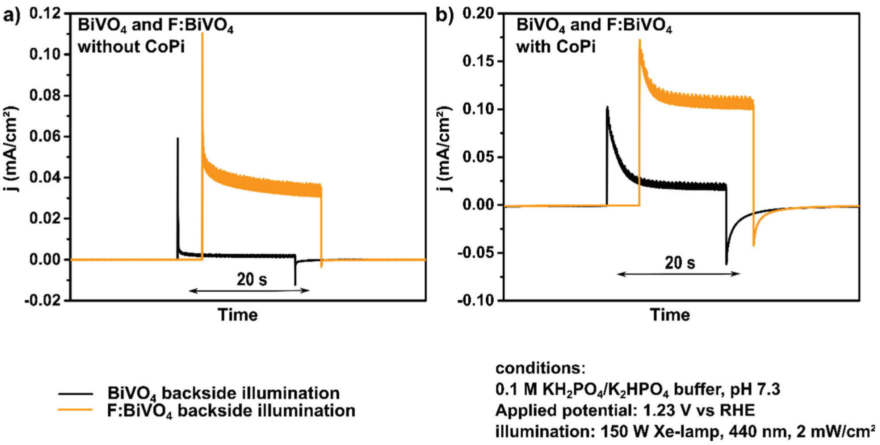

Fig. 15: Photocurrent transients of $BiVO_4$ and F:$BiVO_4$ thin film photoanodes (a) without and (b) with a layer of CoPi deposited, obtained in backside illumination mode. Adapted with permission from ref. [25]. Copyright 2019 American Chemical Society.

are most probably responsible for restrained recombination of photo-generated electron–hole pairs at the surface. In addition, as reported by Wen et al., F also favors water adsorption at the electrode surface, which should have a positive effect on the hole transfer efficiency [46].

After CoPi deposition, spikes and overshoots are still observed for the pristine and the fluorine-containing $BiVO_4$ thin film electrodes (Figure 15b). The transient analysis indicates however a decreased surface recombination upon CoPi deposition for both samples. As such, CoPi enhances water oxidation kinetics by suppressing surface recombination [61, 62], so that the surface-reaching holes are transferred more efficiently to the electrolyte and used for water oxidation undergoing less recombination at the surface.

To disentangle the effects of the fluorination on the PEC performance of $BiVO_4$-based photoanodes further, we estimated the charge-separation efficiency η_{sep} and the catalytic efficiency η_{cat} regarding water oxidation for both samples. As known from literature [19, 63], the total water oxidation photocurrent $J_{\mathrm{H_2O}}$ can be expressed as

$$J_{\mathrm{H_2O}} = J_{\mathrm{abs}} \cdot \eta_{\mathrm{sep}} \cdot \eta_{\mathrm{cat}}$$

with the photon absorption rate J_{abs} given as a current. J_{abs} can be determined by multiplying the emission spectrum of the used light source (150 W Xe lamp, 400–700 nm, intensity adjusted to 100 mW/cm^2) with the absorption spectrum of the thin film electrodes (not shown) and subsequent integration over the wavelength and division by a voltage. By adding sodium sulfite to the electrolyte, which works

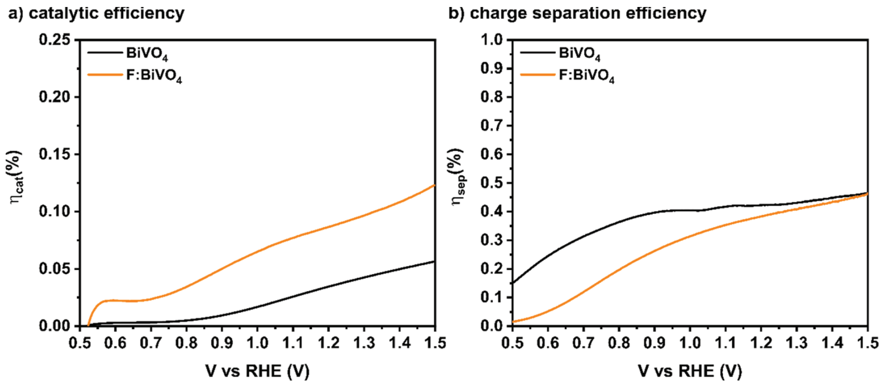

Fig. 16: (a) Catalytic efficiency and (b) charge separation efficiency for $BiVO_4$ and $F:BiVO_4$ thin film photoanodes. Backside illumination was used for recording photocurrents for water oxidation and sulfite oxidation. Adapted with permission from ref. [25]. Copyright 2019 American Chemical Society.

as efficient hole scavenger, surface catalysis efficiency becomes 100% ($\eta_{cat} = 1$) and respective photocurrents (J_{sulfite}) can be used to determine charge separation efficiency and catalytic efficiency via the following equations:

$$\eta_{\text{sep}} = \frac{J_{\text{sulfite}}}{J_{\text{abs}}}$$

$$\eta_{\text{cat}} = \frac{J_{\text{H}_2\text{O}}}{J_{\text{sulfite}}}$$

The catalytic efficiency and charge separation efficiency as a function of applied voltage for $BiVO_4$ and $F:BiVO_4$ thin film electrodes are shown in Figure 16. As can be seen, the catalytic efficiency is significantly enhanced for the fluorinated samples (see Figure 16a), whereas the separation efficiency is slightly decreased for $F:BiVO_4$ thin film samples (see Figure 16b). Therefore, we can conclude that, in good agreement with the photocurrent transient analysis, fluorine modification of $BiVO_4$ improves the hole injection into the electrolyte and hence facilitates the water oxidation at the electrode surface. However, the system still suffers from limited charge separation.

3.3 Mo-doped $BiVO_4$ thin film electrodes

N-type cation doping of $BiVO_4$, i.e. partial substitution of the pentavalent vanadium cation by hexavalent cations like molybdenum or tungsten, was shown by various groups to be a viable method to improve electron transport properties in

$BiVO_4$ [15–17, 64]. We therefore extended our previously presented $BiVO_4$ thin film approach towards the synthesis of Mo-doped $BiVO_4$ thin films with higher PEC water oxidation activity, by the addition of a suitable molybdenum precursor to the precursor solution [18].

The resulting Mo:$BiVO_4$ thin films crystallize in the monoclinic clinobisvanite structure. With increasing Mo content, the crystal structure is transformed into the tetragonal scheelite structure, as was discussed exhaustively in our recently published report [18]. Furthermore, with increasing Mo content within the $BiVO_4$ thin films, the light absorption properties are slightly improved, while the thin films' turbidity increases. This is a consequence of the morphology of the thin films, which is changed upon Mo insertion. As shown for a Mo-doped $BiVO_4$ thin film sample in Figure 17 (10% Mo, see report [18]), the domain size decreases, while the inner material streak size increases when compared to its pristine counterpart. This directly influences the light absorption properties, which are improved upon Mo doping.

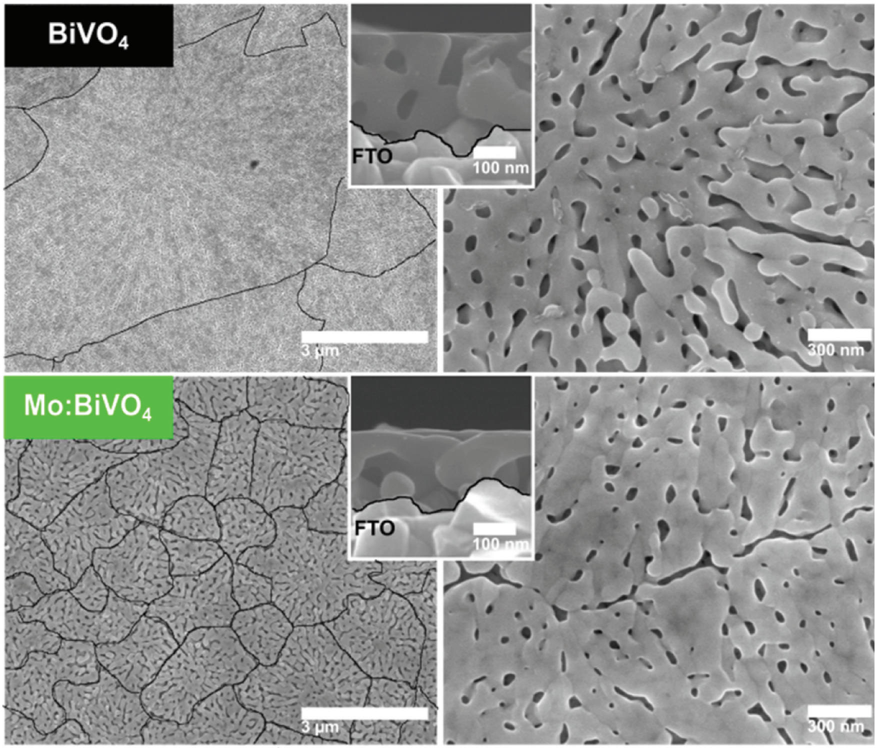

Fig. 17: Top view and cross section images of undoped and Mo-doped $BiVO_4$ thin films on an FTO substrate. Adapted from ref. [18] with permission from The Royal Society of Chemistry.

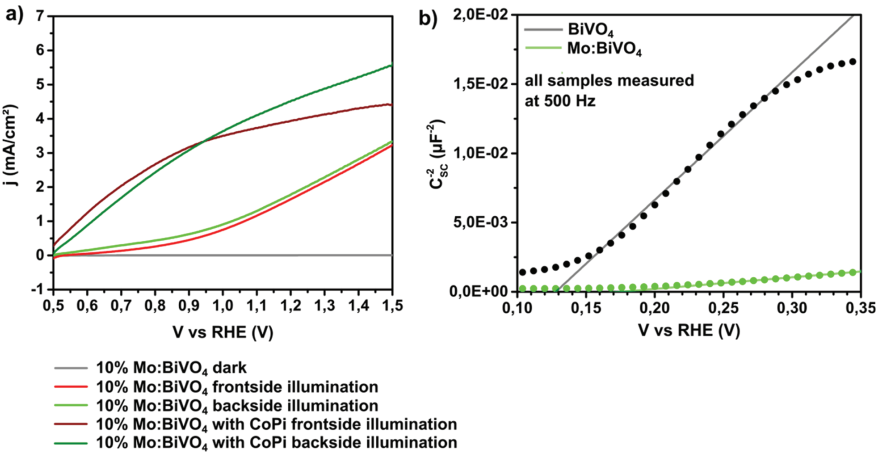

Fig. 18: (a) *j*-*V* curves of a Mo-doped $BiVO_4$ thin film electrode with and without CoPi surface modification in front-side and backside illumination (0.1 m potassium phosphate buffer, pH 7.3, white light [400–700 nm] at 100 mW/cm^2). (b) Mott–Schottky plot for an undoped and Mo-doped $BiVO_4$ thin film electrode (0.5 m potassium phosphate buffer, 20 mV sine modulation).

Investigation of the PEC water oxidation properties of the Mo:$BiVO_4$ thin films revealed drastically improved photocurrents upon Mo incorporation. As can be seen in Figure 18a, photocurrents of 1.9 mA/cm^2 at 1.23 V vs. RHE were observed already before surface modification with a water oxidation catalyst. After CoPi deposition, photocurrents as high as 4.6 mA/cm^2 at 1.23 V vs. RHE were obtained. Additionally, the photocurrents obtained in front-side and backside illumination are very similar, which indicates less charge transport limitation within the electrode material. In addition, Mott–Schottky analysis (shown in Figure 18b) revealed a much smaller slope and a higher density of free charge carriers (electrons) upon Mo-doping of the $BiVO_4$ thin film electrodes.

To gain more information about the effect of Mo incorporation on the PEC performance, the charge-separation efficiency and catalytic efficiency were determined. As can be seen in Figure 19, the charge-separation efficiency is significantly improved via Mo incorporation compared to its unmodified counterpart, while the catalytic efficiency is only slightly improved for Mo-containing $BiVO_4$ electrodes (see Figure 19a).

3.4 Fluorinated Mo-doped $BiVO_4$ thin film electrodes

To enhance the PEC performance of our $BiVO_4$ thin film photoanodes further, concomitant Mo and F incorporation was attempted to combine the enhanced

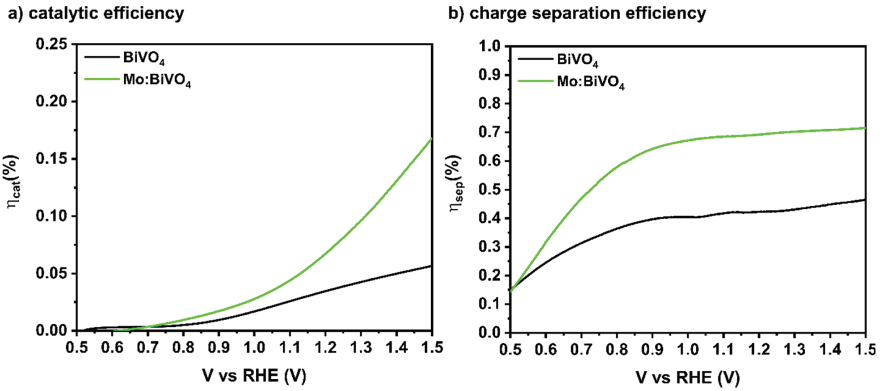

Fig. 19: (a) Catalytic efficiency and (b) charge-separation efficiency for $BiVO_4$ and Mo:$BiVO_4$ thin film electrodes. Backside illumination was used for recording photocurrents for water oxidation and sulfite oxidation.

charge separation due to Mo incorporation with the increased catalytic efficiency due to fluorination. We therefore, as recently reported by us [25], combined both synthetic methods (vide supra) to synthesize a cationic (Mo^{6+}) and anionic (F^-) substituted $BiVO_4$ thin film electrode, referred to as F/Mo:$BiVO_4$. For this purpose, Mo-doped $BiVO_4$ thin films were prepared via the thin-film deposition method explained above. In a second step, the Mo:$BiVO_4$ thin films were fluorinated according to the soft fluorination method developed for powder samples and adjusted to thin film samples, as introduced above.

Structural analysis of the obtained F/Mo:$BiVO_4$ thin films revealed the thin films to crystallize in the clinobisvanite structure favorable for PEC applications (see Figure 20a). No significant change of the crystal structure between Mo:$BiVO_4$ thin films and F/Mo:$BiVO_4$ thin films was observed, which is in good agreement with the findings for F:$BiVO_4$ powder samples and F:$BiVO_4$ thin films. Analysis of the light absorption properties indicated a slight shift of the absorption onset, which indicates a slightly decreased optical band-gap for the F/Mo:$BiVO_4$ thin films compared to its pristine and Mo-doped counterparts (see Figure 20b). Investigations of the thin film morphology showed similar effects in terms of material densification/sintering as shown for the pristine and fluorine-containing $BiVO_4$ thin films (vide supra).

The combination of Mo and F incorporation in $BiVO_4$ thin film electrodes turned out to be very beneficial for the PEC water oxidation properties of the material. As can be seen in Figure 21, higher photocurrents were obtained for the F/Mo:$BiVO_4$ thin films compared to its solely Mo-doped counterparts. Maximum photocurrents of 5.4 mA/cm^2 at 1.23 V vs. RHE were obtained for the F/Mo:$BiVO_4$ thin film electrodes modified with CoPi water oxidation catalyst.

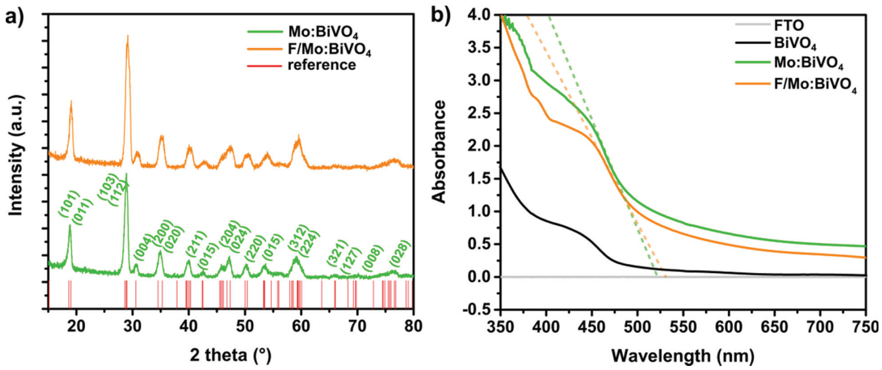

Fig. 20: (a) GI-XRD pattern of a Mo:$BiVO_4$ thin film and an F/Mo:$BiVO_4$ thin film on FTO substrate, (b) UV/Vis spectra of an F/Mo:$BiVO_4$ thin film together with the spectra of corresponding Mo-doped and pristine samples. Adapted with permission from ref. [25]. Copyright 2019 American Chemical Society.

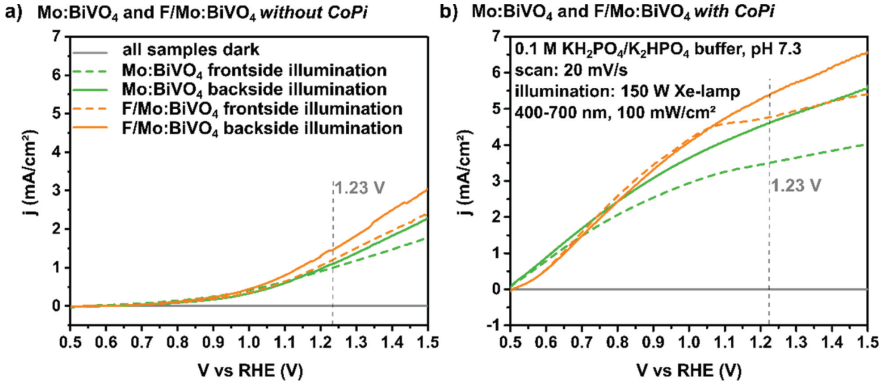

Fig. 21: *j-V* curves of Mo:$BiVO_4$ and F/Mo:$BiVO_4$ thin film photoanodes (a) without CoPi deposited and (b) with CoPi deposited. Adapted with permission from ref. [25]. Copyright 2019 American Chemical Society.

Analysis of charge separation efficiency and catalytic efficiency was carried out to gain insight into the effects of cation-anion co-doping. As can be seen in Figure 22a and b, fluorination predominantly improves hole transfer to the electrolyte (catalytic efficiency), while Mo-incorporation predominantly enhances charge separation efficiency (see Figure 22b).

In this way, we could demonstrate that anion and cation co-doping in $BiVO_4$ allows combining the PEC relevant benefits associated with each type of dopant, thereby improving the PEC water oxidation performance of $BiVO_4$ photoanodes

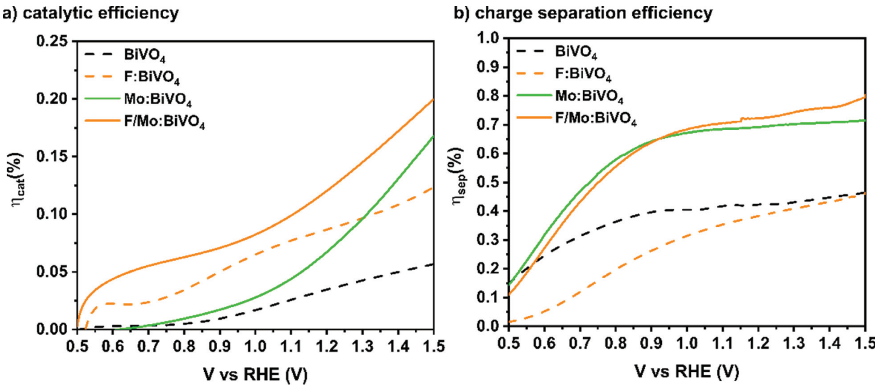

Fig. 22: (a) Catalytic efficiency for $BiVO_4$, Mo:$BiVO_4$, and fluorinated counterparts, (b) charge-separation efficiency for $BiVO_4$, Mo:$BiVO_4$, and fluorinated counterparts. Backside illumination was used for recording photocurrents for water oxidation and sulfite oxidation. Adapted with permission from ref. [25]. Copyright 2019 American Chemical Society.

by enhanced charge separation and improved charge transfer efficiency to the electrolyte.

4 Conclusion

We have presented several strategies to improve the PEC water oxidation performance of $BiVO_4$ photoanodes. First partial O/F-substitution on model $BiVO_4$ powders leading to the creation of cation vacancies was demonstrated to be beneficial for the PEC water oxidation activity of $BiVO_4$ as a result of narrowed optical band gap, increased charge carrier density (n-type doping), cathodically shifted flat-band potential, and decreased surface recombination as well as increased hole transfer efficiency.

Second, in order to optimize the photoanodes' morphology, a novel alkoxide-carboxylate-based synthesis towards *m*-$BiVO_4$-based thin films with improved PEC performance was developed. In addition, improvement of the PEC water oxidation activity could be achieved by partial F/O-substitution, improving the water oxidation kinetics at the electrode surface. Further improvement in terms of charge separation efficiency could be achieved by Mo-doping in the $BiVO_4$ thin films, leading to high water oxidation PEC activities considering the simple single layer electrode design. Finally further improvement of the PEC water oxidation activity could be achieved by anion and cation co-doping, i.e. concomitant partial O/F-substitution and Mo-doping, leading to F/Mo:$BiVO_4$ thin films with increased water oxidation efficiency and increased charge separation efficiency.

Thus, we could reveal that anion and cation co-doping in the present case allows combining the PEC specific benefits of each dopant into one photoanode material.

Acknowledgements: The authors want to thank the Deutsche Forschungsgemeinschaft (DFG) for funding within the priority program SPP 1613 (FI 1885/1-2, LE 781/13-2, SCHE 634/12-2, BR 1768/9-1).

References

1. M. G. Walter, E. L. Warren, J. R. McKone, S. W. Boettcher, Q. Mi, E. A. Santori, N. S. Lewis, Chem. Rev. **110** (2010) 6446.
2. K. Tolod, S. Hernández, N. Russo, Catalysts **7** (2017) 13.
3. Y. Park, K. J. McDonald, K.-S. Choi, Chem. Soc. Rev. **42** (2013) 2321.
4. C. Martinez Suarez, S. Hernández, N. Russo, Appl. Catal. A **504** (2015) 158.
5. J. H. Kim, J. S. Lee, Energy Environ. Focus **3** (2014) 339.
6. Z.-F. Huang, L. Pan, J.-J. Zou, X. Zhang, L. Wang, Nanoscale **6** (2014) 14044.
7. A. Walsh, Y. Yan, M. N. Huda, M. M. Al-Jassim, S.-H. Wei, Chem. Mater. **21** (2009) 547.
8. Z. Zhao, Z. Li, Z. Zou, Phys. Chem. Chem. Phys. **13** (2011) 4746.
9. T. Das, X. Rocquefelte, R. Laskowski, L. Lajaunie, S. Jobic, P. Blaha, K. Schwarz, Chem. Mater. **29** (2017) 3380.
10. F. F. Abdi, T. J. Savenije, M. M. May, B. Dam, R. van de Krol, J. Phys. Chem. Lett. **4** (2013) 2752.
11. Z. Zhao, W. Luo, Z. Li, Z. Zou, Phys. Lett. A **374** (2010) 4919.
12. W.-J. Yin, S.-H. Wei, M. M. Al-Jassim, J. Turner, Y. Yan, Phys. Rev. B **83** (2011).
13. J. Zhang, M. Deng, F. Ren, Y. Wu, Y. Wang, RSC Adv. **6** (2016) 12290.
14. K. Ding, B. Chen, Z. Fang, Y. Zhang, Z. Chen, Phys. Chem. Chem. Phys. **16** (2014) 13465.
15. S. P. Berglund, A. J. E. Rettie, S. Hoang, C. B. Mullins, Phys. Chem. Chem. Phys. **14** (2012) 7065.
16. F. F. Abdi, L. Han, A. H. M. Smets, M. Zeman, B. Dam, R. van de Krol, Nat. Commun. **4** (2013) 2195.
17. H. S. Park, K. E. Kweon, H. Ye, E. Paek, G. S. Hwang, A. J. Bard, J. Phys. Chem. C **115** (2011) 17870.
18. M. Rohloff, B. Anke, S. Zhang, U. Gernert, C. Scheu, M. Lerch, A. Fischer, Sustainable Energy Fuels **1** (2017) 1830.
19. F. F. Abdi, N. Firet, R. van de Krol, ChemCatChem **5** (2013) 490.
20. B. Lamm, B. J. Trześniewski, H. Döscher, W. A. Smith, M. Stefik, ACS Energy Letters **3** (2018) 112.
21. B. J. Trześniewski, W. A. Smith, J. Mater. Chem. A **4** (2016), 2919.
22. Z. Zhao, Z. Li, Z. Zou, RSC Adv. **1** (2011) 874.
23. M. Oshikiri, M. Boero, J. Phys. Chem. B **110** (2006) 9188.
24. B. Anke, M. Rohloff, M. G. Willinger, W. Hetaba, A. Fischer, M. Lerch, Solid State Sci. **63** (2017) 1.
25. M. Rohloff, B. Anke, O. Kasian, S. Zhang, M. Lerch, C. Scheu, A. Fischer, ACS Appl. Mater. Interfaces **11** (2019) 16430.
26. A. W. Sleight, H. Y. Chen, A. Ferretti, D. E. Cox, Mater. Res. Bull. **14** (1979) 1571.

27. F. A. Kröger, H. J. Vink, In: Solid State Phys. Volume 3. F. Seitz, D. Turnbull (Eds.). Academic Press (1956), P. 307.
28. J. J. Mortensen, L. B. Hansen, K. W. Jacobsen, Phys. Rev. B **71** (2005) 4351.
29. J. Enkovaara, C. Rostgaard, J. J. Mortensen, J. Chen, M. Dułak, L. Ferrighi, J. Gavnholt, C. Glinsvad, V. Haikola, H. A. Hansen, H. H. Kristoffersen, M. Kuisma, A. H. Larsen, L. Lehtovaara, M. Ljungberg, O. Lopez-Acevedo, P. G. Moses, J. Ojanen, T. Olsen, V. Petzold, N. A. Romero, J. Stausholm-Møller, M. Strange, G. A. Tritsaris, M. Vanin, M. Walter, B. Hammer, H. Häkkinen, G. K. H. Madsen, R. M. Nieminen, J. K. Nørskov, M. Puska, T. T. Rantala, J. Schiøtz, K. S. Thygesen, K. W. Jacobsen, J. Phys. Condens. Matter **22** (2010) 253202.
30. A. Hjorth Larsen, J. Jørgen Mortensen, J. Blomqvist, I. E. Castelli, R. Christensen, M. Dułak, J. Friis, M. N. Groves, B. Hammer, C. Hargus, E. D. Hermes, P. C. Jennings, P. Bjerre Jensen, J. Kermode, J. R. Kitchin, E. Leonhard Kolsbjerg, J. Kubal, K. Kaasbjerg, S. Lysgaard, J. Bergmann Maronsson, T. Maxson, T. Olsen, L. Pastewka, A. Peterson, C. Rostgaard, J. Schiøtz, O. Schütt, M. Strange, K. S. Thygesen, T. Vegge, L. Vilhelmsen, M. Walter, Z. Zeng, K. W. Jacobsen, J. Phys. Condens. Matter **29** (2017) 273002.
31. V. I. Anisimov, F. Aryasetiawan, A. I. Lichtenstein, J. Phys. Condens. Matter **9** (1997) 767.
32. K. Lai, Y. Zhu, J. Lu, Y. Dai, B. Huang, Solid State Sci. **24** (2013) 79.
33. D. Souri, Z. E. Tahan, Appl. Phys. B Lasers Opt. **119** (2015) 273.
34. A. Kudo, K. Omori, H. Kato, J. Am. Chem. Soc. **121** (1999) 11459.
35. J.-Q. Li, Z.-Y. Guo, H. Liu, J. Du, Z.-F. Zhu, J. Alloys Compd. **581** (2013) 40.
36. H. Jiang, H. Dai, J. Deng, Y. Liu, L. Zhang, K. Ji, Solid State Sci. **17** (2013) 21.
37. A. C. Ulpe, B. Anke, S. Berendts, M. Lerch, T. Bredow, Solid State Sci. **75** (2018) 39.
38. M. Kuisma, J. Ojanen, J. Enkovaara, T. T. Rantala, Phys. Rev. B **82** (2010).
39. M. Rohlfing, S. G. Louie, Phys. Rev. B **62** (2000) 4927.
40. R. Dovesi, A. Erba, R. Orlando, C. M. Zicovich-Wilson, B. Civalleri, L. Maschio, M. Rérat, S. Casassa, J. Baima, S. Salustro, B. Kirtman, WIREs Comput. Mol. Sci. **8** (2018) e1360.
41. A. Erba, J. Phys. Condens. Matter **29** (2017) 314001.
42. T. Bredow, A. R. Gerson, Phys. Rev. B **61** (2000) 5194.
43. M. Hochheim, T. Bredow, Phys. Rev. B **97** (2018) 235447.
44. J. Laun, D. Vilela Oliveira, T. Bredow, J. Comput. Chem. **39** (2018) 1285.
45. M. F. Peintinger, D. V. Oliveira, T. Bredow, J. Comput. Chem. **34** (2013) 451.
46. L. Wen, K. Ding, S. Huang, Y. Zhang, Y. Li, W. Chen, New J. Chem. **41** (2017) 1094.
47. M. I. Aroyo, A. Kirov, C. Capillas, J. M. Perez-Mato, H. Wondratschek, Acta Crystallogr. Sect. A: Found. Crystallogr. **62** (2006) 115.
48. M. I. Aroyo, J. M. Perez-Mato, C. Capillas, E. Kroumova, S. Ivantchev, G. Madariaga, A. Kirov, H. Wondratschek, In: Z. Kristallogr. Vol. 221 (2006), P. 15.
49. M. I. Aroyo, J. M. Perez-Mato, D. Orobengoa, E. Tasci, G. de la Flor, A. Kirov, Bulg. Chem. Commun. **43** (2011) 183.
50. M. W. Kanan, D. G. Nocera, Science **321** (2008) 1072.
51. L. M. Peter, J. Solid State Electrochem. **17** (2013) 315.
52. L. M. Peter, Electroanalysis **27** (2015) 864.
53. L. M. Peter, In: Photocatalysis: Fundamentals and Perspectives, J. Schneider, D. Bahnemann, J. Ye, G. Li Puma, D. D. Dionysiou (Eds.). Royal Society of Chemistry, Cambridge (2016), P. 1.
54. T. W. Kim, K.-S. Choi, Science **343** (2014) 990.

55. B. J. Trześniewski, I. A. Digdaya, T. Nagaki, S. Ravishankar, I. Herraiz-Cardona, D. A. Vermaas, A. Longo, S. Gimenez, W. A. Smith, Energy Environ. Sci. **10** (2017) 1517.
56. D. Wang, R. Li, J. Zhu, J. Shi, J. Han, X. Zong, C. Li, J. Phys. Chem. C **116** (2012) 5082.
57. W. J. Jo, J.-W. Jang, K.-j. Kong, H. J. Kang, J. Y. Kim, H. Jun, K. P. S. Parmar, J. S. Lee, Angew. Chem. Int. Ed. **51** (2012) 3147.
58. J. V. Mantese, A. L. Micheli, A. H. Hamdi, R. W. Vest, MRS Bull. **14** (1989) 48.
59. F. F. Lange, Science **273** (1996) 903.
60. S. Xiao, H. Chen, Z. Yang, X. Long, Z. Wang, Z. Zhu, Y. Qu, S. Yang, J. Phys. Chem. C **119** (2015) 23350.
61. Y. Ma, A. Kafizas, S. R. Pendlebury, F. Le Formal, J. R. Durrant, Adv. Funct. Mater. **26** (2016) 4951.
62. Y. Ma, F. Le Formal, A. Kafizas, S. R. Pendlebury, J. R. Durrant, J. Mater. Chem. A **3** (2015) 20649.
63. H. W. Jeong, T. H. Jeon, J. S. Jang, W. Choi, H. Park, J. Phys. Chem. C **117** (2013) 9104.
64. A. J. E. Rettie, H. C. Lee, L. G. Marshall, J.-F. Lin, C. Capan, J. Lindemuth, J. S. McCloy, J. Zhou, A. J. Bard, C. B. Mullins, J. Am. Chem. Soc. **135** (2013) 11389.